IVYSPRING
INTERNATIONAL PUBLISHER

Theranostics

2018; 8(6): 1591-1606. doi: 10.7150/thno.22430

Research Paper

Bioinspired Multifunctional Melanin-Based Nanoliposome for Photoacoustic/Magnetic Resonance Imaging-Guided Efficient Photothermal Ablation of Cancer

Liang Zhang[1*], Danli Sheng[2*], Dong Wang[1✉], Yuanzhi Yao[3], Ke Yang[1], Zhigang Wang[2], Liming Deng[2], Yu Chen[4✉]

1. Department of Ultrasound, The First Affiliated Hospital of Chongqing Medical University, Chongqing 400016, P. R. China;
2. Institute of Ultrasound Imaging, The Second Affiliated Hospital of Chongqing Medical University, Chongqing, 400010, P. R. China;
3. Department of Ultrasound, Chongqing Cancer Hospital, Chongqing Cancer Institute, Chongqing Cancer Center, Chongqing 400030, P. R. China;
4. State Key Laboratory of High Performance Ceramics and Superfine Microstructures, Shanghai Institute of Ceramics, Chinese Academy of Sciences, Shanghai, 200050, P. R. China.

* These two authors contributed equally to this work.

✉ Corresponding authors: D. Wang (wang57554@163.com); Y. Chen (chenyu@mail.sic.ac.cn)

Received: 2017.08.18; Accepted: 2017.12.08; Published: 2018.02.07

Abstract

Background: The construction of theranostic nanosystems with concurrently high biosafety and therapeutic performance is a challenge but has great significance for the clinical translation of nanomedicine for combating cancer.

Methods: Bio-inspired melanin-based nanoliposomes (Lip-Mel) as theranostic agents were constructed for simultaneous photoacoustic (PA) imaging- and T_1-weighted magnetic resonance (MR) imaging-guided photothermal ablation of tumors, which was demonstrated both *in vitro* and *in vivo*. The high biosafety of Lip-Mel was also systematically evaluated.

Results: The achieved Lip-Mel nanoliposomes demonstrated their imaging capability for both PA and T_1-weighted MR imaging (r_1 = 0.25 $mM^{-1} \cdot s^{-1}$) both *in vitro* and *in vivo*, providing the potential for therapeutic guidance and monitoring. Importantly, the desirable photothermal-conversion efficiency of the as-prepared Lip-Mel achieved complete eradication of tumors in breast cancer-bearing mice, exhibiting remarkable photothermal-based therapeutic performance. In particular, the efficient encapsulation of melanin into the PEGylated liposome mitigated the potential toxicity of melanin and improved the photothermal performance of the loaded melanin. Systematic *in vivo* biosafety evaluations demonstrated the high biocompatibility of Lip-Mel at a high dose of 100 mg/kg.

Conclusion: In this work, we reported a bioinspired strategy where melanin, a natural product in the human body, is encapsulated into PEGylated nanoliposomes for efficient theranostics with high biocompatibility. This work provides a new strategy for creating desirable theranostic agents with concurrent high biocompatibility and satisfactory theranostic performance through the use of materials that totally originate from biosystems.

Key words: Melanin, Liposome, Photoacoustic imaging, MRI, Photothermal ablation, Nanomedicine

Introduction

Theranostic nanomedicine has been developing rapidly for early diagnosis and efficient therapy of cancer in the past decades [1-4]. A large number of inorganic, organic, and organic-inorganic hybrid theranostic nanoagents have been explored for versatile biomedical applications, including gold nanoparticles (Au NPs) [5, 6], quantum dots (QDs) [7, 8], India ink [9], superparamagnetic iron oxide (SPIO) [10, 11], carbon-based nanomaterials [12, 13], synthetic dye-based nanocarriers (e.g., ICG, IR780) [14-17], etc. As these nanoagents are optical absorbers, when stimulated by laser irradiation at specific wavelengths, they can generate noninvasive photoacoustic contrast enhancement, heat tissues to higher temperatures, and even cause thermal damage. However, the further clinical implementation of these nanoagents is hindered by biosafety issues because of their poor biodegradability and unclear biocompatibility [18, 19]. To solve this critical biosafety issue, theranostic nanoplatforms synthesized from endogenous ingredients from living organisms have attracted tremendous attention in theranostic nanomedicine for further clinical translation [20-22].

Melanin, mainly presenting in the skin, hair follicles and eyes, is an endogenous biological pigment with intrinsic optical absorption capability [23, 24]. Recent progress has preliminarily demonstrated that melanin-based nanoparticles could serve as multifunctional contrast agents for both photoacoustic imaging (PAI) [25-27] and magnetic resonance imaging (MRI) [26-29]. Such melanin-based contrast agents possess desirable biosafety and mitigate side effects. Therefore, a melanin-based nanoplatform with endogenous composition could show great promise in diagnostic imaging based on its optical properties and satisfactory biocompatibility.

Photothermal therapy (PTT) is a noninvasive therapeutic modality for tumor therapy, featuring a short recovery period, low recurrence rate, and real-time temperature monitoring, showing superior characteristics compared to conventional surgery and chemotherapy [30, 31]. Typically, within the tumor tissue, PTT agents absorb near infrared (NIR) light and convert light energy into heat, eventually leading to irreversible cell damage (apoptosis and coagulative necrosis of tumor cells) and tumor ablation [30-32]. In particular, melanin, as a potential PTT agent, has demonstrated high photothermal conversion efficiency [33]; but, melanin delivery has not been satisfactorily effective to achieve high PTT efficiency.

Nanoliposomes, as a potential drug carrier nanosystem, have the advantages of tunable drug loading, easy metabolism, prolonged biological half-life and low toxicity [34, 35]. In particular, PEGylation of liposomes (PEG: polyethylene glycol) can increase the bioavailability of drugs or nanoagents by overcoming the critical issue of quick elimination by the mononuclear phagocyte system (MPS) in systemic circulation [36], minimize toxicity or side effects of nanoagents by prolonging their circulation and increase the passive accumulation of delivered therapeutic agents [37, 38].

To develop a novel melanin-based theranostic nanomedicine, we herein successfully constructed melanin-based nanoliposome-PEG (Lip-Mel) by a facile trichloromethane-injection and freeze-drying strategy. Melanin was entrapped in nanoliposome-PEG to mitigate its toxicity, improve phagocytosis by tumor cells and enhance the PTT effect. The physiochemical properties of Lip-Mel were systematically characterized. In particular, these Lip-Mel nanosystems were developed as contrast agents for dual-mode contrast-enhanced PAI and MRI, providing the potential for therapeutic guidance and monitoring. The high photothermal-conversion efficiency of Lip-Mel successfully achieved efficient ablation of tumor tissue.

Materials and Methods

Materials

Melanin and propidium iodide (PI) were purchased from Sigma Aldrich (St. Louis, MO, USA). 1,2-dipalmitoyl-sn-glycero-3-phosphatidylcholine (DPPC), 1,2-distearoyl-sn-glycero-3-phosphoethanolamine-N-[methoxy (polyethylene glycol)-2000] (DS PE-mPEG2000) and cholesterol were purchased from Avanti Polar Lipids, Inc. (Alabaster, AL, USA). Calcein acetoxymethyl ester (Calcein-AM) was purchased from Santa Cruz Biotechnology (TX, USA). Cell Counting Kit-8 (CCK-8) was purchased from Dojindo (Japan). 1,1'-dioctadecyl-3,3,3',3'-tetramethylindocarbocyanine perchlorate (DiI), 2-(4-Amidinophenyl)-6-indolecarbamidinedihydrochloride (DAPI) and 1,1′-dioctadecyl-3,3,3′,3′-tetramethylindotricarbocyanine iodide (DiR) were obtained from Beyotime Technology. Deionized water was obtained from a Millipore water purification system. All reagents were used without further purification.

Synthesis of Lip-Mel and Lip

Lip-Mel and Lip were prepared by a trichloromethane-injection and freeze-drying strategy. First, a certain mass of hybrid lipid (12 mg DPPC, 4 mg DSPE-mPEG2000 and 4 mg cholesterol) was dissolved into 20 mL trichloromethane ($CHCl_3$). Melanin granule (2 mg) was dissolved in 5 mL ammonium hydroxide ($NH_3 \cdot H_2O$), and then ammonia was volatilized completely by rotary evaporation in a water bath at 55 °C. The prepared melanin solution (2 mL) was then transferred into a 100 mL round-bottomed flask in a water bath at 65 °C with a magnetic stirrer. Then, the trichloromethane-lipid solution was contained into a 20 mL syringe and was added dropwise into the above melanin aqueous solution at a flow rate of 0.1 mL/min monitored by a high-precision syringe pump (Baoding Longer Precision Pump Co., Ltd, China). After the removal of the trichloromethane, self-assembled phospholipids formed the liposomes with melanin aqueous solution in the core. The formed melanin-loaded liposome was then homogenized using an ultrasonic probe (Sonics & Materials Inc., USA) at 100 W for 2 min. The resulting nanoparticles were further purified with a centrifugal filter (MWCO = 100 kDa). After centrifugation (1300 xg, 10 min), deionized water was added into the centrifugal filter. Then, a pipette was used to aspirate up and down to re-disperse the liposomes. The centrifugation-washing step was repeated five times. Finally, the final nanoliposomes were lyophilized and Lip-Mel powder was stored at room temperature for further use. Pure liposome (Lip) powder was prepared using a similar process, except 2 mL deionized water was added instead of the melanin aqueous solution during the synthesis.

Characterization of Lip-Mel

The morphology of Lip-Mel was observed by an optical microscope (Olympus DP70, Canada). The nanostructure of Lip-Mel was analyzed by a transmission electron microscope (TEM, Hitachi H-7600, Japan) after negative staining with sodium phosphotungstate solution (2%, w/w). A Laser Particle Size Analyzer System (Nano, ZS90, Malvern instrument Ltd) was used to determine the size distribution and zeta-potential of Lip-Mel and Lip. The particle size of Lip-Mel dispersed in phosphate buffered saline (PBS) was recorded at different time points (0 d, 1 d, 3 d, 7 d and 14 d). The UV-Vis-NIR absorption spectrum of melanin was recorded using a UV-Vis-NIR spectrophotometer (UV-3600, Shimadzu, Japan) at room temperature. A standard concentration curve of free melanin aqueous solution at a wavelength of 715 nm was measured to determinate the amount of melanin encapsulated into liposomes. Melanin entrapment content and efficiency were calculated by the following equations:

Melanin entrapment content (%) = (Mass of melanin in composite liposomes/Mass of Lip-Mel) × 100 %

Melanin entrapment efficiency (%) = (Mass of melanin in composite liposomes/Total melanin inputs) × 100%

To measure the melanin release profiles, Lip-Mel dispersed in PBS was dialyzed against a 100 k MWCO membrane, and rotated at 37 °C, 120 rpm. At the predetermined time points (2 h, 4 h, 6 h, 8 h, 12 h, 1 d, 3 d, 5 d, 7 d and 14 d), the releasing solution was taken out to test the melanin concentration by a UV-Vis-NIR spectrophotometer.

Cell culture and MDA-MB-231 tumor-bearing mice model

The human breast cancer MDA-MB-231 cell line was obtained from Institute of Ultrasound Imaging, Chongqing Medical University (Chongqing, China) and cultured in high glucose dulbecco's modified eagle medium (DMEM) supplemented with 10% fetal bovine serum (FBS) and 1% penicillin-streptomycin solution in a humidified atmosphere of 5% CO_2 at 37 ^{o}C. When the cultured cells reached 80% confluency, they were sub-cultured at a ratio of 1:3 for cell experiments and construction of tumor models.

All animals (female BALB/c nude mice and BALB/c mice: ~20 g, 4-6 weeks) were purchased from the Experimental Animal Center of Chongqing Medical University. All the experiments and procedures were performed under guidelines approved by the Institutional Animal Care and Use Committee at Chongqing Medical University. To establish MDA-MB-231 tumor-bearing mice models, MDA-MB-231 cells were suspended into serum-free DMEM ($1×10^6$ MDA-MB-231 cells in 100 μL per mouse) and then injected subcutaneously into the flanks of the female BALB/c nude mice. The volume of the tumor was calculated as [$\pi/6 \times \text{length} \times (\text{width})^2$]. The BALB/c mice were used for biosafety evaluation of Lip-Mel, Lip and melanin.

Cytotoxicity of Lip-Mel

To evaluate the cytotoxicity of Lip-Mel, Lip and free melanin, MDA-MB-231 cells were seeded into a 96-well plate ($1×10^4$ cells per well) overnight. After cell adhesion, Lip-Mel dispersed in serum-free DMEM solution was added into each well at different concentrations (0.00, 0.40, 0.80, 1.20, 1.60 and 2.00 mg/mL). The toxicities of Lip and free melanin were also tested as the control groups. The concentrations of Lip and melanin corresponded to their content in Lip-Mel. After another 24 h co-incubation, cell viabilities were tested by the typical CCK-8 assay. Five replicates were conducted for each group.

Biosafety evaluation of Lip-Mel, Lip and melanin

BALB/c mice (~20 g, 4-6 weeks) were randomly divided into thirteen groups as follows: control, 1 d Lip-Mel, 1 d Lip, 1 d melanin, 3 d Lip-Mel, 3 d Lip, 3 d melanin, 7 d Lip-Mel, 7 d Lip, 7 d melanin, 14 d Lip-Mel, 14 d Lip and 14 d melanin (n = 5 per group), which were then intravenously injected with saline solution (control group), Lip-Mel (100 mg/kg), Lip, and free melanin suspension (groups of 1, 3, 7, 14 days post intravenous injection). The concentrations of Lip and melanin corresponded to their content in Lip-Mel. The behaviors of the mice during the evaluation were monitored. The blood samples and major organs (heart, liver, spleen, lung and kidney) were collected after 1 day (control group and 1 d group), 3 days (3 d group), 7 days (7 d group) or 14 days (14 d group) feeding post injection. The blood samples were collected for serum biochemical indexes analysis and routine blood examination. The serum biochemical indexes included aspartate aminotransferase (AST), alanine aminotransferase (ALT), total bilirubin (TBIL), blood urea nitrogen (BUN), creatinine (CR), creatine kinase (CK) and L-lactate dehydrogenase (LDH-L) The major organs were stained with H&E (hematoxylin and eosin) for histological analysis.

In vivo biodistribution

For *in vivo* biodistribution of Lip-Mel, MDA-MB-231 tumor-bearing mice (n = 4) were intravenously injected with DiR-labeled Lip-Mel saline solution (10 mg/mL, 200 µL). Fluorescence images were acquired pre, 1 h, 3 h, 6 h, 24 h and 48 h post injection, and the relative fluorescence intensities within the tumor regions were measured. The major organs and tumor of one mouse were harvested for *ex vivo* fluorescence imaging.

In vitro and *in vivo* PAI

For evaluating the PA performance of Lip-Mel, a Vevo LAZR Photoacoustic Imaging System (VisualSonics Inc., Toronto, Canada) equipped with a LZ250 (fiber-optic bundles: 25.4 × 1.25 mm; focal depth: 10 mm; center frequency: 21 MHz; axial resolution: 75 µm) probe was used to acquire PA and ultrasound images. Lip-Mel suspension at a concentration of 3 mg/mL was scanned for PAI at different wavelengths ranging from 680 nm to 970 nm (interval = 5 nm) to detect the maximum absorbance for optimized PAI. The quantified PA signal intensities within a region of interest (ROI) of each image were then analyzed by Vevo LAZR software. Different concentrations of Lip-Mel dispersed in PBS ranging from 0 to 5 mg/mL were triggered by the optimal excitation wavelength to acquire the corresponding PA images. In addition, PA images of 3 mg/mL Lip-Mel suspension were obtained at different time points (0 h, 6 h, 12 h and 24 h) for photostability analysis. The PA intensities of each image were measured.

For the *in vivo* PA imaging, MDA-MB-231 tumor-bearing mice (n = 3) were intravenously injected with 200 µL Lip-Mel at a dose of 10 mg/mL. Then, PA images were collected at different time points (pre, 1 h, 4 h and 24 h) and average PA intensities in the tumor regions were measured.

Evaluations of the magnetic properties of Lip-Mel and MRI *in vitro* and *in vivo*

The magnetic properties of Lip-Mel and melanin powder were tested by Physical Property Measurement System (PPMS) at 300 K. All MR imaging experiments were conducted on a 7.0 T micro-MRI System (Bruker, Pharmascan) equipped with a small animal-specific coil. Lip (10 mg/mL), and Lip-Mel dispersed in PBS at different concentrations (0-10 mg/mL) were placed in 2 mL Eppendorf tubes for T_1-weighted and T_1 mapping MRI. The imaging parameters for the T_1-weighted MRI were set as follows: fast field echo (FFE), TR = 600.0 ms, TE = 6.0 ms, flip = 45°, FOV = 180 mm, and slice thickness = 1.0 mm. The imaging parameters for the T_1 mapping MRI were set as follows: TR = 400.0 ms, 800.0 ms, 1200.0 ms, 2400.0 ms, 3600.0 ms, 4800.0 ms, TE = 8.0 ms, slice thickness = 1.0 mm, FOV = 180 mm. The MRI signal intensity (SI) and relaxation time T_1 within the region of interest (ROI) were measured.

Mice were injected subcutaneously with Lip-Mel suspension at concentrations of 0, 2, 4, 6, 8 and 10 mg/mL for further sensitivity detection of Lip-Mel for MRI. Average SI of the Lip-Mel-injected regions and buttocks muscles were measured five times to calculate the intensity ratio (Lip-Mel/muscle).

For *in vivo* MRI, MDA-MB-231 tumor-bearing mice (n = 3) were intravenously injected with 200 µL Lip-Mel at a dose of 10 mg/mL. Then, T_1-weighted MR images were collected at different time points (pre, 1 h, 4 h and 24 h) and pseudo-coloring was applied to each image using Matlab (2016). The method of self-controlled study was used to evaluate the *in vivo* MRI effect. Average MRI signal intensity (SI) in the tumor region (SI_{tumor}) and buttocks muscles (SI_{muscle}) of the same slice were measured. Relative signal intensity (SIr) and the percentage of signal intensity increase (PSII) were calculated.

$$SIr = SI_{tumor}/SI_{muscle}$$

$$PSII = (SIr_{post} - SIr_{pre}) / SIr_{pre} \times 100\%$$

In vitro photothermal properties of Lip-Mel

In vitro photothermal property of Lip-Mel was evaluated by laser irradiation of Lip-Mel at different concentrations. 808 nm laser was adopted for photothermal evaluation. In addition, different power densities of the 808 nm laser were introduced for irradiation. Water, Lip and melanin were used as controls. The temperature changes and infrared radiation (IR) thermal images were recorded by an infrared thermal-imaging camera (Fotric 226).

Intracellular uptake of Lip-Mel and *in vitro* photothermal ablation against MDA-MB-231 cells

The intracellular uptake of Lip-Mel was detected by confocal laser scanning microscopy (CLSM) (Nikon A1, Japan). Typically, MDA-MB-231 cells (2×10^4) were seeded into a laser confocal cell culture dish. After 24 h incubation, the culture medium was replaced with the medium containing Lip-Mel (labeled with DiI, $\lambda_{excitation}/\lambda_{emission}$=549 nm/565 nm). After another 12 h co-incubation, the nuclei of MDA-MB-231 cells were stained by blue DAPI ($\lambda_{excitation}/\lambda_{emission}$=340 nm/488 nm). The fluorescence images were directly recorded by CLSM.

The MDA-MB-231 cancer cells were seeded in 96-well plates (1×10^4 cells per well) overnight. After cell adhesion, Lip-Mel-serum-free-DMEM solution was added into each well at different melanin concentrations. After another 12 h of incubation, the cells were exposed to an 808 nm laser for 5 min at different power densities. Five replicates were conducted for each group. Finally, the cell viabilities were determined by CCK-8 assay.

For confocal observation, the MDA-MB-231 cancer cells were seeded onto four confocal-specific cell-culture dishes (1×10^5 cells per dish; four groups: control, Lip-Mel only, Laser only and Lip-Mel + Laser) overnight. After cell adhesion, Lip-Mel suspension was added into two dishes (two groups: Lip-Mel only, Lip-Mel + Laser) and equal volume serum-free DMEM was added into the other two dishes. After another 12 h of incubation, cells of two groups (Laser only and Lip-Mel + Laser) were irradiated by an 808 nm laser for 5 min at a power density of 1.50 W/cm^2. Then, the medium was removed and the cells of each dish were washed three times with PBS. The living cells and dead cells were co-stained with calcein-AM and PI solution for confocal observation.

In vivo photothermal ablation against tumor-bearing mice assisted by Lip-Mel

For evaluating the *in vivo* photothermal efficiency of Lip-Mel, twenty-four MDA-MB-231 tumor-bearing mice were used when the tumor volumes reached about 100 mm^3. The mice were divided into four groups (6 mice per group) randomly. The first group was set as the control group, which was intravenously injected with saline solution (200 μL). The second group was Lip-Mel only group intravenously receiving Lip-Mel suspension (200 μL) at a concentration of 10 mg/mL. The third group was the Laser only group, which was intravenously injected with saline solution (200 μL) followed by 808 nm laser exposure for 10 min at a power density of 1.50 W/cm^2. The fourth group was Lip-Mel + Laser group, which was intravenously injected with Lip-Mel suspension (10 mg/mL, 200 μL) followed by 808 nm laser exposure for 10 min at a power density of 1.50 W/cm^2. After intravenous injection, the mice were anesthetized for PTT evaluation. The temperature and IR thermal images were recorded by an infrared thermal-imaging camera. The tumor-volume change of four groups was monitored with a digital camera and the weight of each mouse was recorded every other day after PTT. The tumor-volume changes were normalized using the relative tumor volumes V/V_0 (V_0: the initial tumor volume before the treatment). One mouse of each group was sacrificed 24 h post treatment, and the main organs (heart, liver, spleen, lung and kidney) and the tumor issues were collected and fixed in a 4% paraformaldehyde solution. Finally, the main organs were stained with H&E, and the tumor tissues were stained with H&E, TdT-mediated dUTP Nick-End Labeling (TUNEL) and Ki-67 for histopathology analysis.

Statistical analysis

All statistical analyses were performed with SPSS 20.0 software. Data is presented as mean ± standard deviation. The significance of the data was analyzed according to Student's *t* test: $^*P < 0.05$, $^{**}P < 0.01$.

Results and discussion

Design, synthesis and characterization of Lip-Mel

Lip-Mel, a unique core/shell structure nanoparticle with liposome-PEG as the shell and melanin granule as the core, was engineered for imaging-guided photothermal ablation of tumors. These Lip-Mel can efficiently accumulate into the tumor region *via* the typical enhanced permeability and retention (EPR) effect during blood circulation **(Figure 1)**. After entering the tumor site, these Lip-Mel act as contrast agents for concurrent PAI and MRI, providing guidance for the following photothermal ablation and potential for evaluating the therapeutic outcome. Upon external NIR laser irradiation, these Lip-Mel can behave as photothermal conversion agents for increasing the tumor temperature and ablating the tumor cells/tissues.

Nano-sized and phospholipid-coated liposome-PEG containing melanin core was fabricated by the self-assembly of melanin and hybrid lipid, followed by a post freezing-dry process **(Figure 2A and Figure S1)**. This strategy could directly encapsulate the melanin into the nanoliposome with high efficiency and expose the lip-PEG shell to aqueous solution for enhanced stability in physiological condition. The obvious color change **(Figure S2A, B)** from the white powder of Lip to the dark brown powder of Lip-Mel indicated the successful encapsulation of melanin. Figure **2B** shows the morphology and dispersity of Lip-Mel, which feature a uniform size/shape and high dispersity, as observed by bright-field optical microscopy. A TEM image of Lip-Mel **(Figure 2C)** presents the microstructure of Lip-Mel, showing a uniform spherical morphology with a homogeneous distribution of melanin within the matrix. The average hydrodynamic diameters of Lip-Mel and Lip were determined to be 300.5 nm (PDI = 0.187) and 299.3 nm (PDI = 0.104), respectively, which were measured by the typical dynamic light scattering (DLS) method **(Figure 2D)**. The size of Lip-Mel was almost unchanged after encapsulation of melanin as compared with Lip. The Lip-Mel dispersion exhibited a more negative zeta potential compared to Lip (**Figure S2C**). This is likely because the DSPE-PEG does not fully cover the surface of the liposome, causing a negatively charged surface. In addition, the slightly slow diffusion of melanin from Lip-Mel onto the surface was hypothesized to change the surface status of the nanoliposome, causing a more negatively charged surface. The freeze-dried powders of Lip-Mel could also be easily dispersed into aqueous solution for further biomedical use **(Figure 2D inset)**. Therefore, Lip-Mel represents a novel organic bio-inspired multifunctional theranostic agent having all components originating from the natural human body for efficient cancer imaging and treatment.

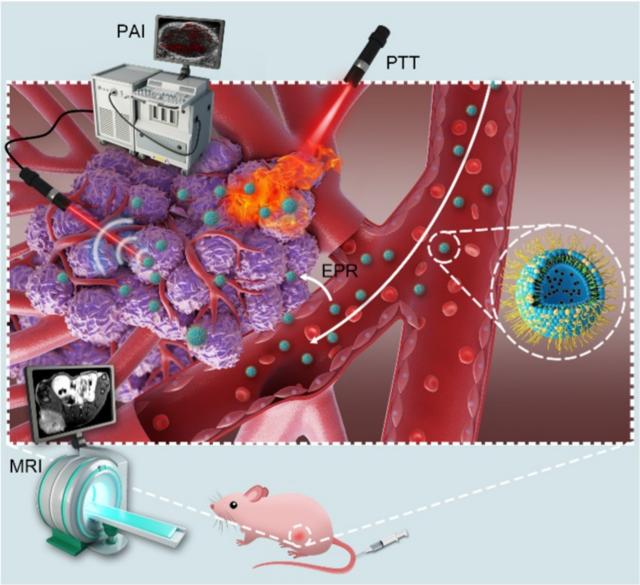

Figure 1. Schematic illustration of the theranostic functions of as-synthesized Lip-Mel, including their passive accumulation into the tumor tissue *via* the typical EPR effect followed by PA/MR imaging-guided PTT ablation of the tumor.

The size change of Lip-Mel and the accumulated release of melanin from Lip-Mel were further monitored for a two-week period. It was found that the size remained almost unchanged during the two-week period **(Figure 2E)**, suggesting the high stability of Lip-Mel in physiological condition to some extent. Less than 40% of melanin was released during the two-week period **(Figure S3)**, which is believed to be sufficiently long for the therapeutic purposes. The optical property of melanin was further characterized by UV-Vis-NIR absorption spectroscopy **(Figure 2F)**. Melanin showed a concentration-dependent increase in absorbance intensity, which represented a linear relationship at 715 nm and 808 nm, as described by the following linear correlation equations: $Y = 0.001X + 0.0296$ ($R^2 = 0.9944$, 715 nm) and $Y = 0.0004X + 0.0195$ ($R^2 = 0.9935$, 808 nm) **(Figure 2G)**. The melanin-entrapment amount in Lip-Mel was calculated by a weight ratio (melanin/Lip-Mel) of 90.9 μg/mg and the melanin-encapsulation efficiency was 89.5%.

In vitro cytotoxicity and *in vivo* biosafety assay of Lip-Mel

The biocompatibility and biosafety of Lip-Mel are of high significance for further clinical translation, and so were systematically evaluated both *in vitro* and *in vivo*. The cytotoxicities of Lip-Mel, Lip and melanin were evaluated by the typical CCK-8 assay. The resulting cell viability suggested no obvious cytotoxicity for Lip-Mel and Lip in the analyzed concentration range, even at the high concentration up to 2.00 mg/mL of Lip-Mel **(Figure 3A)**. Comparatively, melanin showed hypotoxicity with the elevated concentration. For instance, the cell viability was 95.37% for Lip-Mel at a concentration of 0.40 mg/mL, but the cell viability decreased significantly to 62.92% for pure melanin. This result demonstrated that the encapsulation of melanin into liposomes can substantially decrease the cytotoxicity of melanin, which is of high importance for safe theranostic biomedical applications. The *in vivo* biocompatibility was further evaluated in mice after the intravenous administration of Lip-Mel, Lip and melanin for prolonged durations (1 d, 3 d, 7 d and 14 d). No obvious abnormal behaviors were found among all mice, suggesting that Lip-Mel, Lip and melanin did not cause significant side effects to the mice. The blood indexes including liver functional markers (ALT, AST, TBIL), kidney functional markers (BUN, CR), myocardial enzyme spectrum (CK, LDH-L) and complete blood count (RBC, WBC, PLT, HGB, etc.) showed negligible variation among the different groups, indicating undetectable toxicity in short and relatively long timeframes **(Figure 3B,**

Figure S4-5). Although Lip-Mel, Lip and melanin also accumulated in the liver and kidneys, negligible liver and kidney damage was induced. H&E staining of the major organs (heart, liver, spleen, lung and kidney) at different durations after intravenous injection showed no significant acute or chronic physiological toxicity as compared with the control group **(Figure 3C, Figure S6-18)**, indicating the high histocompatibility of Lip and melanin. These preliminary *in vivo* results indicate that the as-synthesized Lip-Mel has high *in vivo* biocompatibility. Lipid and melanin are both endogenous ingredients [24, 39], which guarantees that they can be potentially metabolized normally.

In vivo bio-distribution

We then used fluorescence imaging to track the *in vivo* delivery and bio-distribution of Lip-Mel. Fluorescence images were acquired at set time points after intravenous injection of DiR-labeled Lip-Mel. As shown in **Figure S19A, B**, fluorescence signals within the tumor region behaved in a time-dependent manner. The peak value of fluorescence signals at the tumor site was recorded at 24 h post injection. The *ex vivo* fluorescence images of the major organs and tumor at 24 h post injection (**Figure S19C, D**) suggested the effective accumulation of Lip-Mel into tumor tissue for effective cancer theranostics.

In vitro and *in vivo* photoacoustic imaging

Inspired by the desirable photo-absorption in the NIR region, as reflected in most excellent PAI-based contrast agents [40, 41], Lip-Mel was further evaluated to determine its diagnostic-imaging performance for PAI. As shown in **Figure 4A,** 700 nm was determined to be the maximum absorbance for the potentially optimal PAI. The B-mode ultrasound images, PA images and overlay images (B-mode and PA mode) of Lip and Lip-Mel suspension at elevated concentrations are shown in **Figure 4B**. It was found that Lip-Mel showed the concentration-dependent contrast enhancement in PAI while the pristine Lip represented no contrast change even at high concentration, indicating that the encapsulated melanin contributed to the PA signal enhancement.

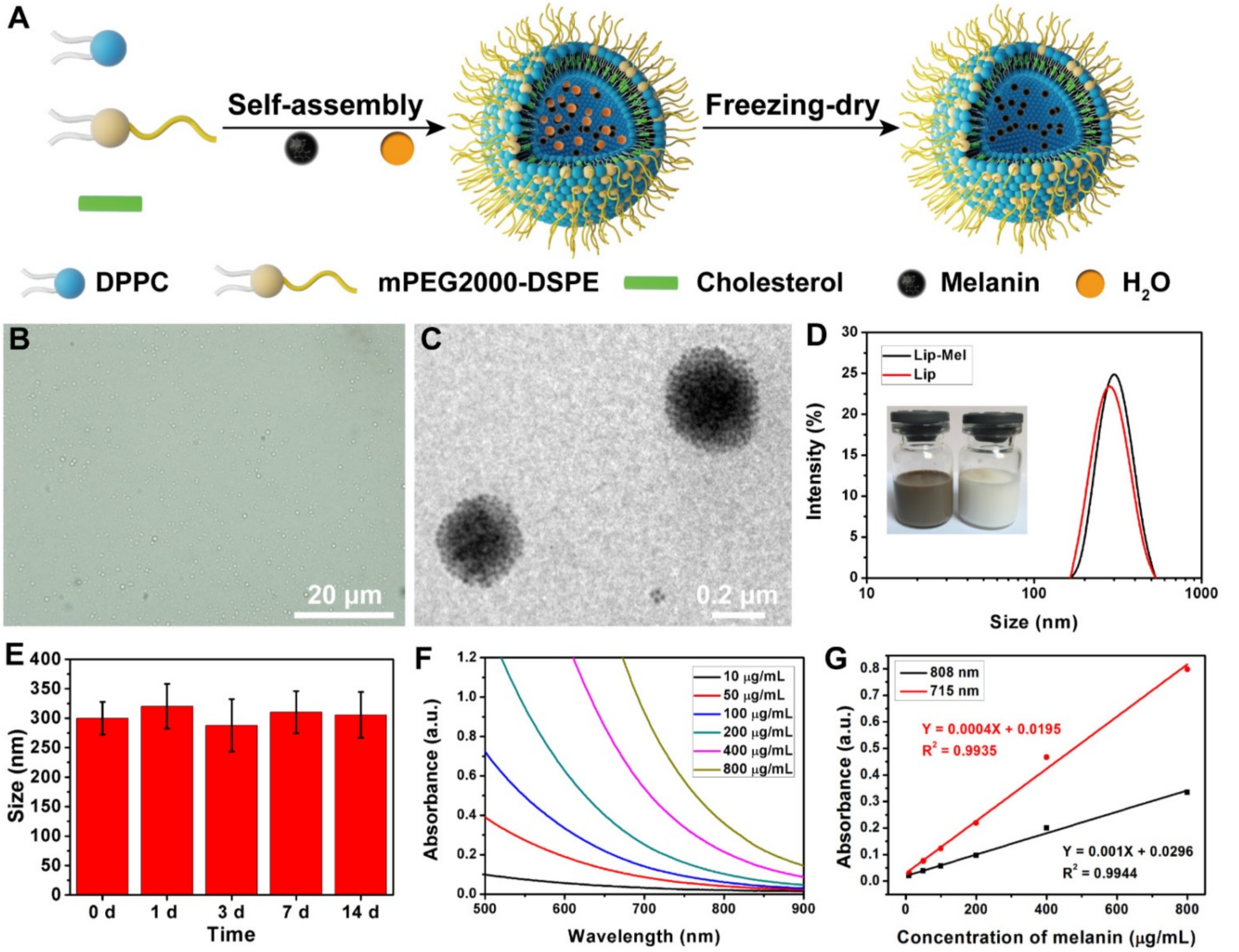

Figure 2. (**A**) Schematic illustration of the synthetic procedure of Lip-Mel. (**B**) Bright-field optical microscopy image (scale bar = 20 μm) and (**C**) TEM image (scale bar = 0.2 μm) of Lip-Mel. (**D**) Size distribution of Lip-Mel and Lip (Inset: photographs of Lip-Mel and Lip dispersed in deionized water). (**E**) Particle-size change of Lip-Mel with prolonged time. (**F**) UV-Vis-NIR absorbance spectra of melanin at varied concentrations. **(G)** The concentration-dependent absorbance of melanin in the UV-Vis-NIR region at the wavelengths 808 nm and 715 nm.

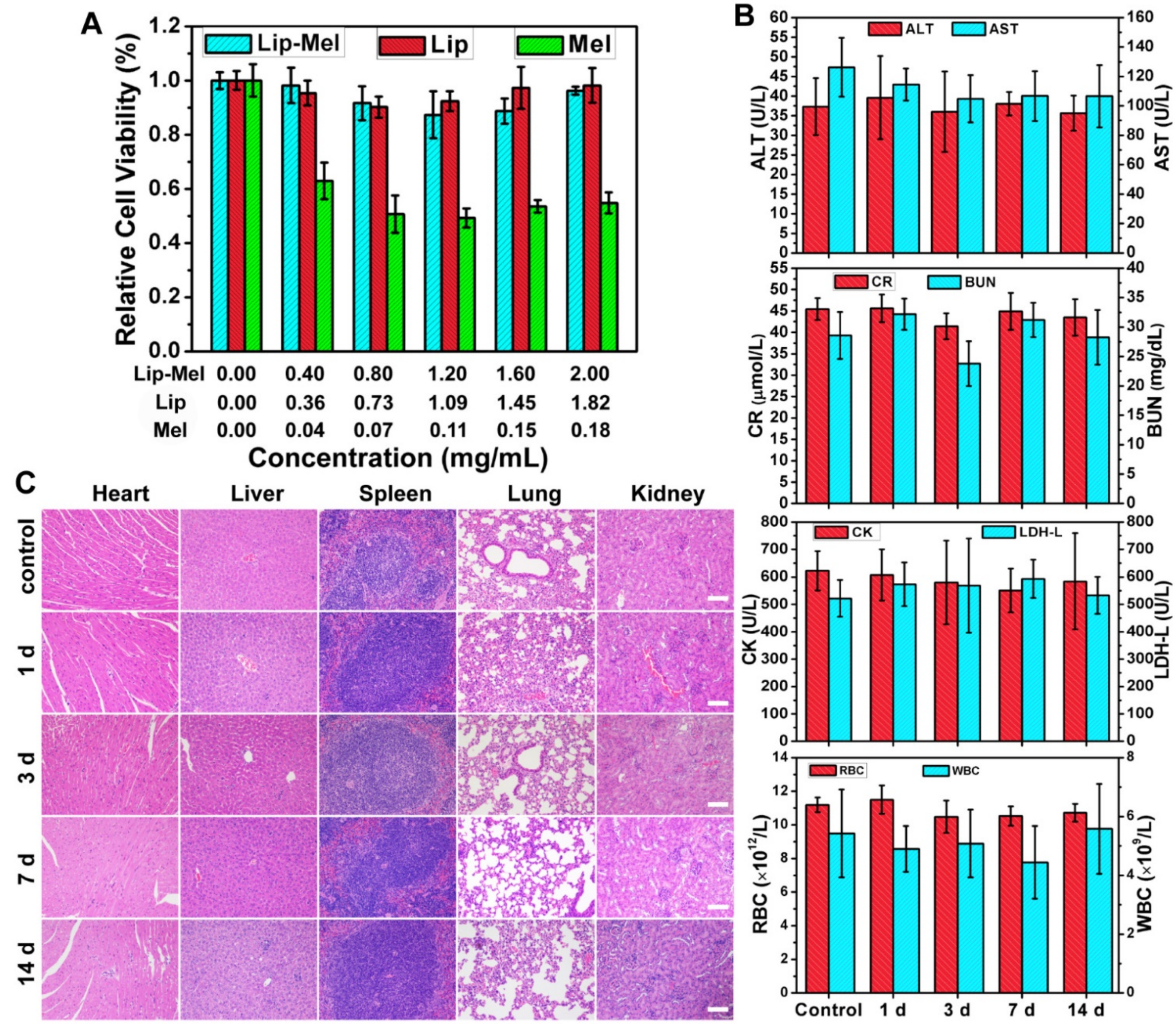

Figure 3. *In vitro* cytotoxicity and *in vivo* biosafety assay of Lip-Mel. (**A**) Cell cytotoxicity of Lip-Mel, Lip and Melanin after co-incubation with MDA-MB-231 cells for 24 h. The concentrations of Lip and melanin corresponded to their content in Lip-Mel. (**B**) Hematological assay of BALB/c mice and (**C**) H&E staining of major organs from the control group and the experimental groups 1, 3 ,7, 14 days post intravenous injection of Lip-Mel. All the scale bars are 100 μm.

Quantitative PA signal intensities increased linearly relative to elevated Lip-Mel concentration **(Figure 4C)**. Furthermore, PA images of Lip-Mel suspension (3 mg/mL) were obtained with prolonged time, and the PA signal had no obvious change, indicating the high stability of Lip-Mel for PAI performance **(Figure 4D)**. Different from many photosensitizers, which are easily degraded due to their low photostability, Lip-Mel could keep its photostability for potentially continuous PAI. The *in vivo* PAI performance of Lip-Mel was further evaluated in tumor-bearing mice. The *in vivo* PA images showed that the PA signal increased gradually with prolonged observation **(Figure 4E)** after the intravenous administration of Lip-Mel (10 mg/mL, 200 μL), indicating the gradual accumulation of Lip-Mel within the tumor region. The PA signal enhancement was further quantitatively analyzed by the PA signal intensities in the ROI **(Figure 4F)**. PAI modality has been proven to be a practical method for noninvasive melanoma imaging of over-expressed melanin [42, 43]. Therefore, Lip-Mel could be used as exogenous PA contrast agent for diagnostic imaging of other organs and diseases as well.

In vitro and *in vivo* T_1-weighted MRI

It is very intriguing that melanin itself can act as the contrast agent for enhanced T_1-weighted MRI [44-46]. Magnetism of Lip-Mel and melanin was further assessed by Physical Property Measurement

System (PPMS). The magnetic hysteresis curves at 300 K (**Figure S20**) confirmed the paramagnetic behavior of Lip-Mel and melanin, which showed magnetization saturation values of 0.06 and 0.29 emu/g, respectively. Given their paramagnetic behavior, such a multifunctional Lip-Mel was expected to enhance the contrast of positive MR imaging. To demonstrate this assumption, T_1-weighted and T_1 mapping MRI were conducted on Lip (10 mg/mL), PBS, and Lip-Mel dispersed in PBS at different concentrations. It has been found that brighter T_1-weighted MR images of Lip-Mel suspension were detected with increased Lip-Mel concentrations, indicating the capability of our Lip-Mel to enhance T_1-weighted MRI **(Figure 5A inset)**. T_1 values were then plotted as relaxation $1/T_1$, which increased with a good linear relationship vs. Lip-Mel concentration **(Figure 5A)**. As shown in **Figure S21**, the longitudinal relativity r_1 was calculated to be 0.25 $mM^{-1}\cdot s^{-1}$, which is lower than that of commercial Gd^{3+} chelates (r_1 = 3.8 $mM^{-1}\cdot s^{-1}$) [47]. However, these Lip-Mel nanoliposomes without metal ions have their own characteristic performances that traditional Gd-based agents do not have. For instance, they can be used for photothermal ablation of tumors. They can also be employed for PA imaging. The contrast-enhanced MRI performance of Lip-Mel nanoliposomes can be used for therapeutic guidance and monitoring during photothermal ablation, though their MR imaging performance is lower as compared to clinically used Gd-based agents.

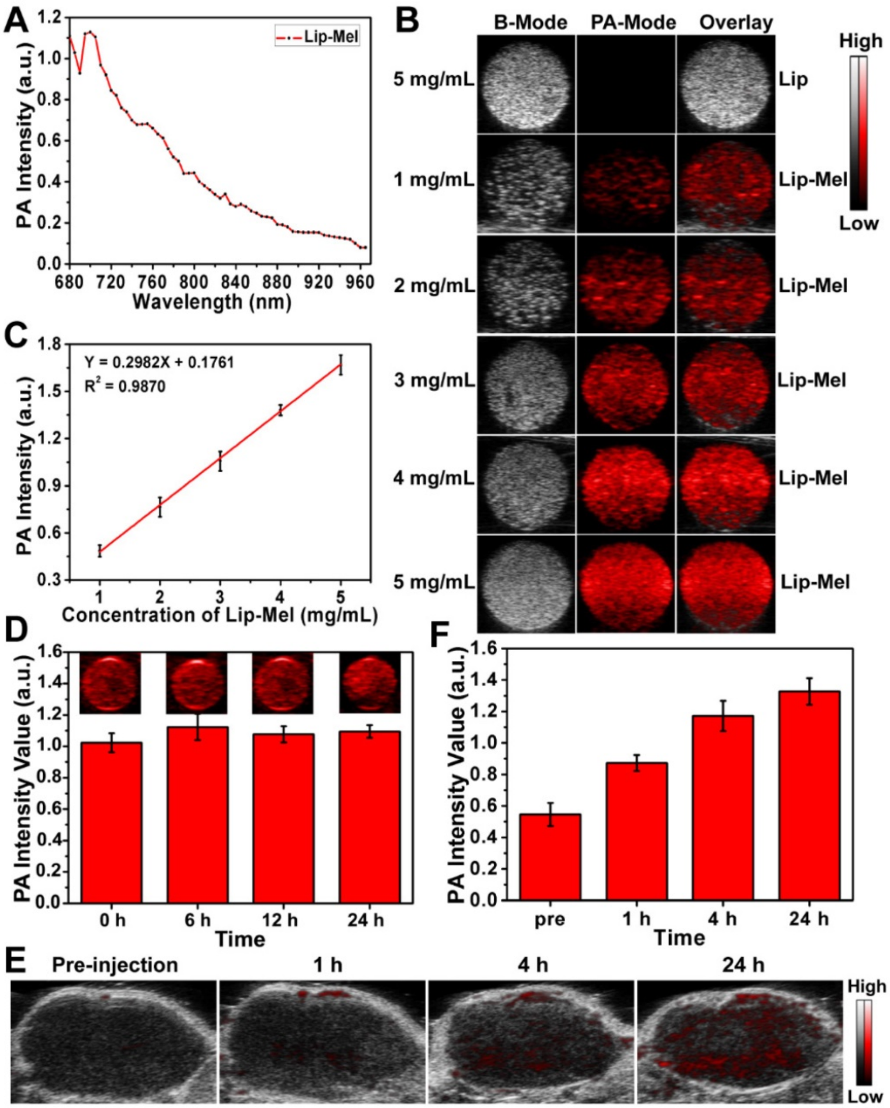

Figure 4. *In vitro* and *in vivo* PAI assessment of Lip-Mel. (**A**) PA spectrum of Lip-Mel (3 mg/mL) from 680 nm to 970 nm. (**B**) PAI of Lip at a concentration of 5 mg/mL and Lip-Mel at concentrations of 1, 2, 3, 4, 5 mg/mL (from top to bottom). (**C**) Quantitative PA signal intensities versus Lip-Mel concentration curve. (**D**) Photo-stability analysis of Lip-Mel for PAI: PA images (inset images) of Lip-Mel and quantitative PA intensity changes at a concentration of 3 mg/mL with prolonged imaging. (**E**) PAI of MDA-MB-231 tumor before and after (1 h, 4 h and 24 h) intravenous injection of Lip-Mel and **(F)** corresponding quantitative analysis of enhanced PA signal intensities (n = 3, mean ± SD).

The *in vivo* paramagnetic sensitivity for T_1-weighted imaging was then assessed by subcutaneous injection of Lip-Mel at different concentrations on the back of living mice **(Figure S22A)**, and the average MR SI of the Lip-Mel-injected region and buttock muscles were measured. Relative MR SI (ratio = Lip-Mel/muscle) increased versus Lip-Mel concentration **(Figure S22B)**. The diagnostic imaging of tumor was further assessed on tumor-bearing mice by intravenous administration of Lip-Mel. As shown in **Figure 5B**, an obvious bright effect could be detected at the tumor region over time after intravenous injection of Lip-Mel, and pseudo-coloring of grayscale images was performed to further clearly show the enhancement in MRI signal. PSII was used for quantitative analysis of MRI signal intensity with prolonged observation, which showed gradual positive signal enhancement over time **(Figure 5C)**, consistent with fluorescence imaging and PAI. Therefore, the as-prepared Lip-Mel could act as contrast agent for positive T_1-weighted MR imaging of tumors.

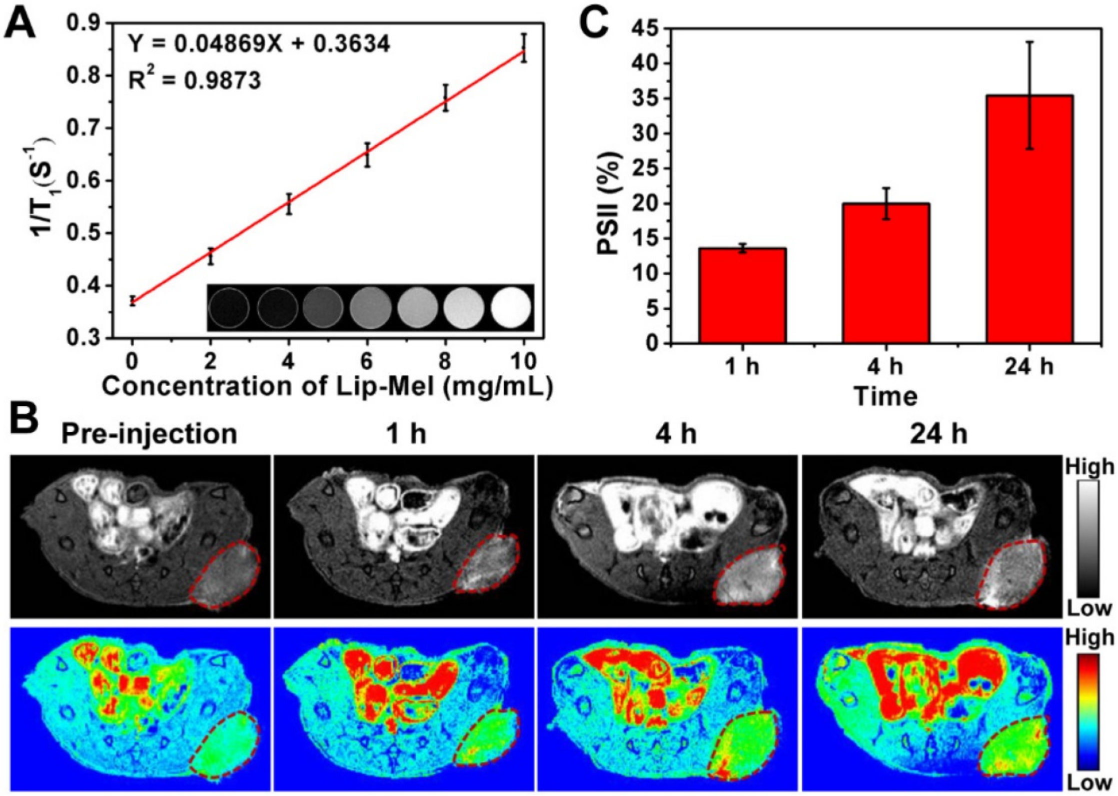

Figure 5. *In vitro* and *in vivo* MRI assessment of Lip-Mel. (**A**) The curve of $1/T_1$ versus Lip-Mel concentration under T_1-weighted MRI scanning. Inset: T_1-weighted MRI of Lip at a concentration of 10 mg/mL and Lip-Mel at concentrations of 0, 2, 4, 6, 8 and 10 mg/mL (from left to right). (**B**) MRI of MDA-MB-231 tumor-bearing mice (region enveloped by red dotted line) before and after (1 h, 4 h and 24 h) intravenous injection of Lip-Mel (TR 600.0 ms, TE 6.0 ms). The top row shows grayscale images, and the bottom row shows the pseudo-coloring images. (**C**) Quantitative analysis of enhanced MR signal intensities in MDA-MB-231 tumor over time after intravenous injection of Lip-Mel (n = 3, mean ± SD).

Based on the absorption of melanin in the NIR bio-window, real-time optoacoustic imaging technology could identify the specific signal generated from melanin with pseudo color in the anatomical position of a living animal, showing high imaging effect in tracing tumors. Therefore, melanin can serve as an ideal target for both PAI and MRI. With its noninvasive, accurate and dynamic features, PAI provides functional and molecular information of the tumor with high sensitivity [48-50]. MRI provides high spatial resolution imaging and anatomical information of diseases but suffers from low temporal resolution. The combination of PAI and MRI renders simultaneously dynamic and anatomical information in diagnosis [51]. Therefore, the presented results suggest that Lip-Mel can act as an efficient contrast agent of both PAI and MRI for further therapeutic guidance and monitoring.

In vitro and *in vivo* photothermal ablation of cancer cells and tumor

The photo-absorption capability of Lip-Mel in the NIR range endows it with therapeutic capabilities for photothermal ablation. To assess the PTT efficiency, Lip-Mel at varied melanin concentrations (45.45 90.90, 181.80, 363.60 μg/mL) was exposed to an 808 nm laser at a power density of 1.50 W/cm² **(Figure 6A, S23)**. At the melanin concentration of 363.60 μg/mL, the suspension temperature increase could reach as high as 51.5 °C within 5 min of NIR irradiation. In contrast, the temperature of pure water showed almost no temperature increase, indicating that the presence of Lip-Mel can efficiently and rapidly convert NIR light into thermal energy. More detailed experiments were performed to investigate the photothermal performance of Lip-Mel at varied concentrations under a laser power density of 1.00 W/cm² **(Figure S24A)** and the corresponding infrared radiation (IR) thermal images were obtained **(Figure S24B)**. In addition, the temperature increases and IR thermal images of Lip-Mel at different laser power densities (0.75, 1.00, 1.25, 1.50 W/cm²) were collected **(Figure 6B, S25)**. The temperature increased significantly with the elevation of NIR irradiation power. The photothermal effect of Lip-Mel depended on both concentration and laser power density. To further evaluate the photothermal stability of Lip-Mel, the cyclical temperature change of Lip-Mel suspension was recorded under 808 nm laser irradiation at a power density of 1.50 W/cm² **(Figure 6C)** and 1.00 W/cm² **(Figure S26)** for 5 min (laser on), followed by natural cooling to room temperature (laser off) for five laser on/off cycles. The photothermal performance of Lip-Mel did not show any obvious decay during the irradiation cycling, underlining the potential of Lip-Mel as a reusable photothermal nanoagent. Moreover, it was found that Lip-Mel triggered a remarkable temperature increase (ΔT = 51.5 °C, **Figure 6D, S27**), which was higher than that of free melanin (ΔT = 42.7 °C) and Lip (ΔT = 2.4 °C). Obviously, Lip-Mel exhibited higher photothermal-conversion efficiency over free melanin. Currently, there are very few strategies to improve the photothermal-conversion efficiency of organic molecules [52]. This work demonstrated that the design of core/shell-structured Lip-Mel could improve the photothermal performance of loaded melanin molecules. It is hypothesized that by liposomal confinement, melanin has a more concentrated distribution as compared to free melanin. In addition, the lipid shell cannot attenuate the laser. Once the laser irradiation is absorbed by melanin inside the liposome, the energy could be more easily transmitted to nearby liposome-confined melanin units rather than resulting in energy loss to the solvent.

Lip-Mel was further used as the photothermal agent for *in vitro* ablation against MDA-MB-231 breast cancer cells upon exposure to 808 nm laser. Efficient intracellular uptake of Lip-Mel could improve the PTT efficiency for killing the cancer cells. MDA-MB-231 cells were incubated with Lip-Mel to evaluate the intracellular uptake of the particles. It was found that Lip-Mel could be efficiently endocytosed into MDA-MB-231 cells **(Figure 7A)**, as demonstrated by the strong red fluorescence from DiI-labeled Lip-Mel. Typically, liposomes are effectively endocytosed into cancer cells *via* the clathrin-mediated endocytosis process [53], which could enhance the intracellular accumulation of melanin, facilitating the following therapeutic process.

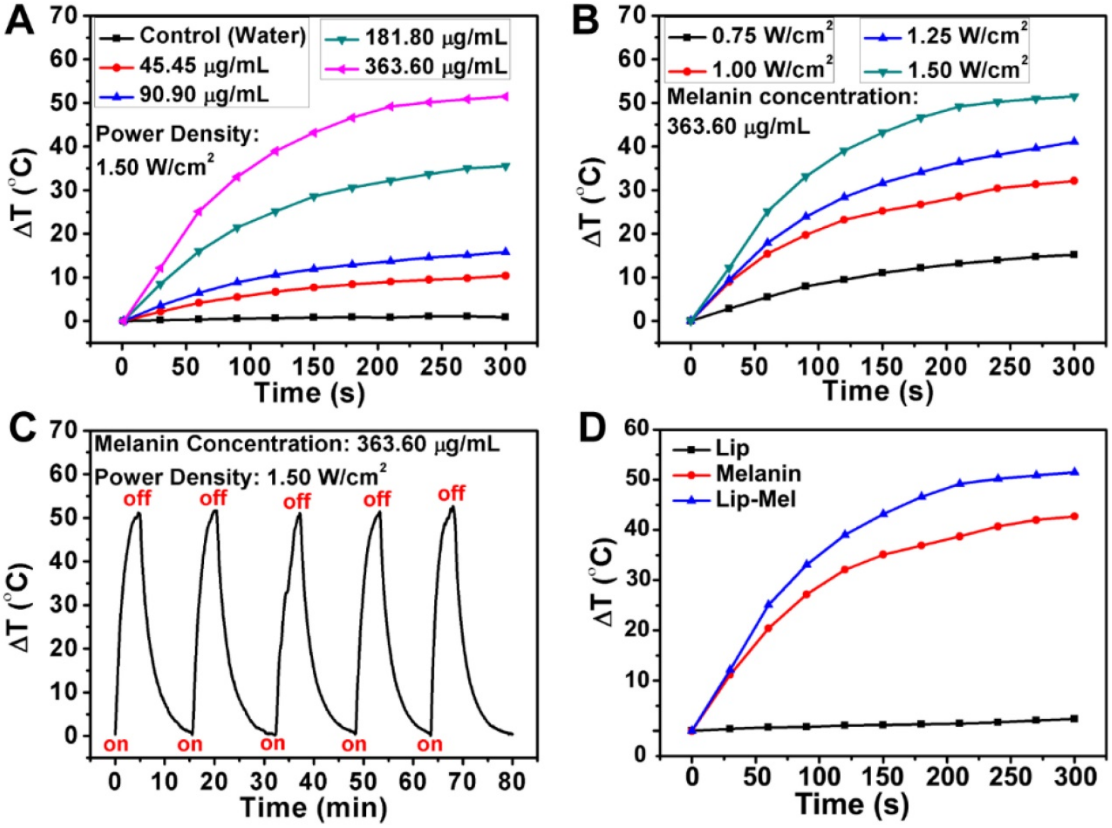

Figure 6. *In vitro* solution-based photothermal performance of Lip-Mel. (**A**) Plot of temperature change (△T) of pure water and Lip-Mel suspension at different concentrations (45.45, 90.90, 181.80, 363.60 μg/mL) as a function of irradiation duration using an 808 nm laser (1.50 W/cm²). (**B**) Plot of temperature change (△T) of Lip-Mel suspension at different power densities of an 808 nm laser (0.75, 1.00, 1.25 and 1.50 W/cm² as a function of irradiation duration (melanin concentration: 363.60 μg/mL, 100 μL). (**C**) Cycled heating profiles of Lip-Mel (melanin concentration: 363.60 μg/mL, 100 μL) irradiated by an 808 nm laser (1.50 W/cm²) for five laser on/off cycles. (**D**) Plot of temperature change (△T) of Lip-Mel (melanin concentration: 363.60 μg/mL), melanin (363.60 μg/mL) and Lip suspension as a function of irradiation duration using an 808 nm laser (1.50 W/cm²).

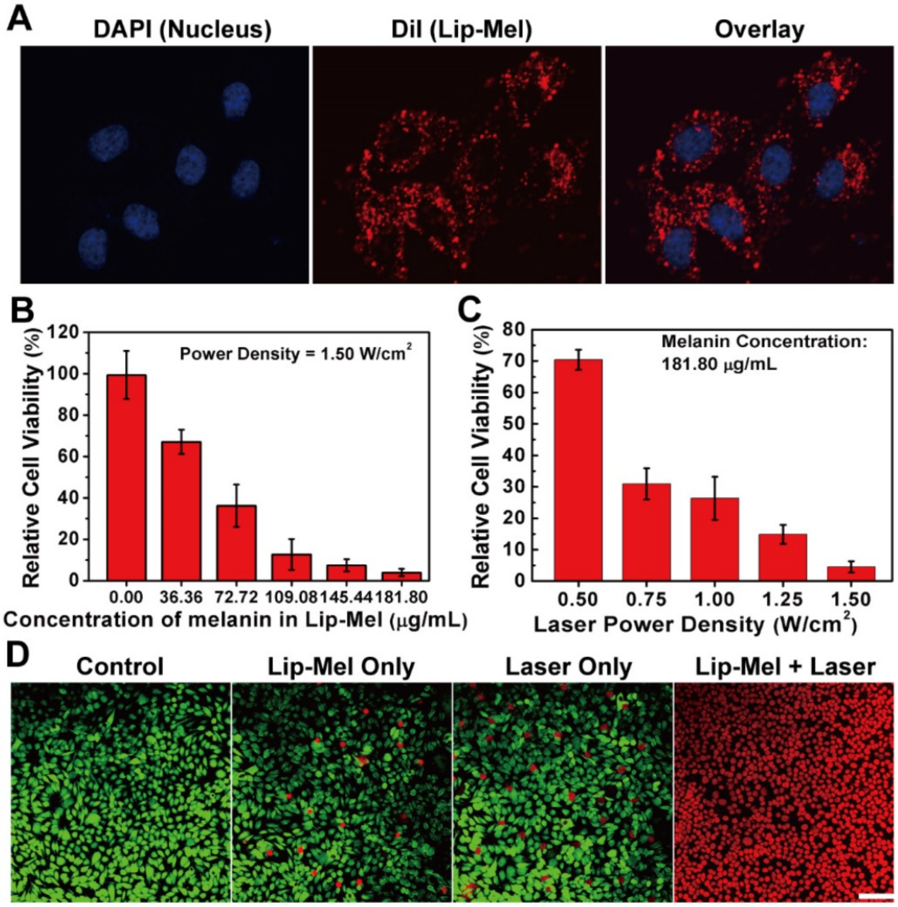

Figure 7. Intracellular uptake of Lip-Mel and *in vitro* photothermal ablation of cancer cells. (**A**) Intracellular uptake of Lip-Mel as observed by CLSM. The images from left to right show cell nuclei stained by DAPI, Lip-Mel stained by DiI, and the overlay of the two fluorescence images; (**B**) Cell viabilities of MDA-MB-231 cells after co-incubation with elevated melanin concentrations (0.00, 36.36, 72.72, 109.08, 145.44 and 181.80 μg/mL) in Lip-Mel followed by NIR irradiation (1.50 W/cm²) for 5 min. (**C**) Cell viabilities of MDA-MB-231 cells after incubation with Lip-Mel (181.80 μg/mL of melanin in Lip-Mel) followed by NIR irradiation at different laser power densities (0.50, 0.75, 1.00, 1.25, and 1.50 W/cm². (**D**) Confocal fluorescence imaging of Calcein AM and PI co-stained MDA-MB-231 cells after co-incubation with Lip-Mel for 12 h followed by different treatments (scale bar = 100 μm).

MDA-MB-231 cells were co-incubated with Lip-Mel suspension at different melanin concentrations and then irradiated with an 808 nm laser at a power density of 1.50 W/cm². It was found that the cell viability decreased with elevated melanin concentrations upon external laser irradiation **(Figure 7B)**. Additionally, MDA-MB-231 cells were irradiated with a laser at elevated power densities. Together with the increase in laser energy, more cancer cells incubated with Lip-Mel were killed by the laser irradiation **(Figure 7C)**. *In vitro* photothermal ablation of MDA-MB-231 cells was further detected by CLSM. No dead cells were found in the control group, showing the green fluorescence of Calcein AM staining. Negligible dead cells were found in the Laser only and Lip-Mel only groups, as indicated by the strong green fluorescence and very weak red fluorescence of PI staining. In contrast, in the Lip-Mel + Laser group, all the cells showed a strong red fluorescence, indicating the presence of large numbers of dead cells due to the photothermal ablation induced by Lip-Mel under external NIR irradiation **(Figure 7D)**.

Encouraged by the *in vitro* PTT efficacy of Lip-Mel, an *in vivo* PTT experiment was carried out by the intravenous injection of Lip-Mel. MDA-MB-231 tumor-bearing mice were divided into four groups (n = 6), including groups of control, Laser only, Lip-Mel only, and Lip-Mel + Laser. Based on the *in vivo* biodistribution of Lip-Mel, Lip-Mel passively accumulated in the tumor region and reached a peak accumulation at 24 h post injection, consistent with the previous report [54]. Therefore, the mice were anesthetized for PTT at 24 h post injection. The temperature and IR thermal images were recorded by an infrared thermal imaging camera. As shown in **Figure 8A** and **Figure S28**, the surface temperature of tumors in the Lip-Mel + Laser group increased from 23.8 ± 1.2 °C to 51.1 ± 2.5 °C under irradiation for 10 min, which was sufficient to ablate the tumor tissue [55, 56]. Comparatively, the temperature at the tumor region of mice in the Laser only group showed only a slight temperature change. Two days after PTT, the tumor tissues in the Lip-Mel + Laser group were necrotic, leaving black scars in the initial tumor regions **(Figure 8B)**. After twenty days, the black scar disappeared, leaving the complete eradication of tumor **(Figure 8C)**. In contrast, tumors of the other three groups grew significantly. The tumor-volume changes of the four groups were monitored and the weight of each mouse was recorded every other day. Then, the tumor-volume change was normalized using relative tumor volumes of V/V_0 **(Figure 8D)**. Remarkably, the tumors of mice in Lip-Mel + Laser group were ablated completely, demonstrating the high PTT efficiency of Lip-Mel. In comparison, the tumors of the other three groups grew rapidly.

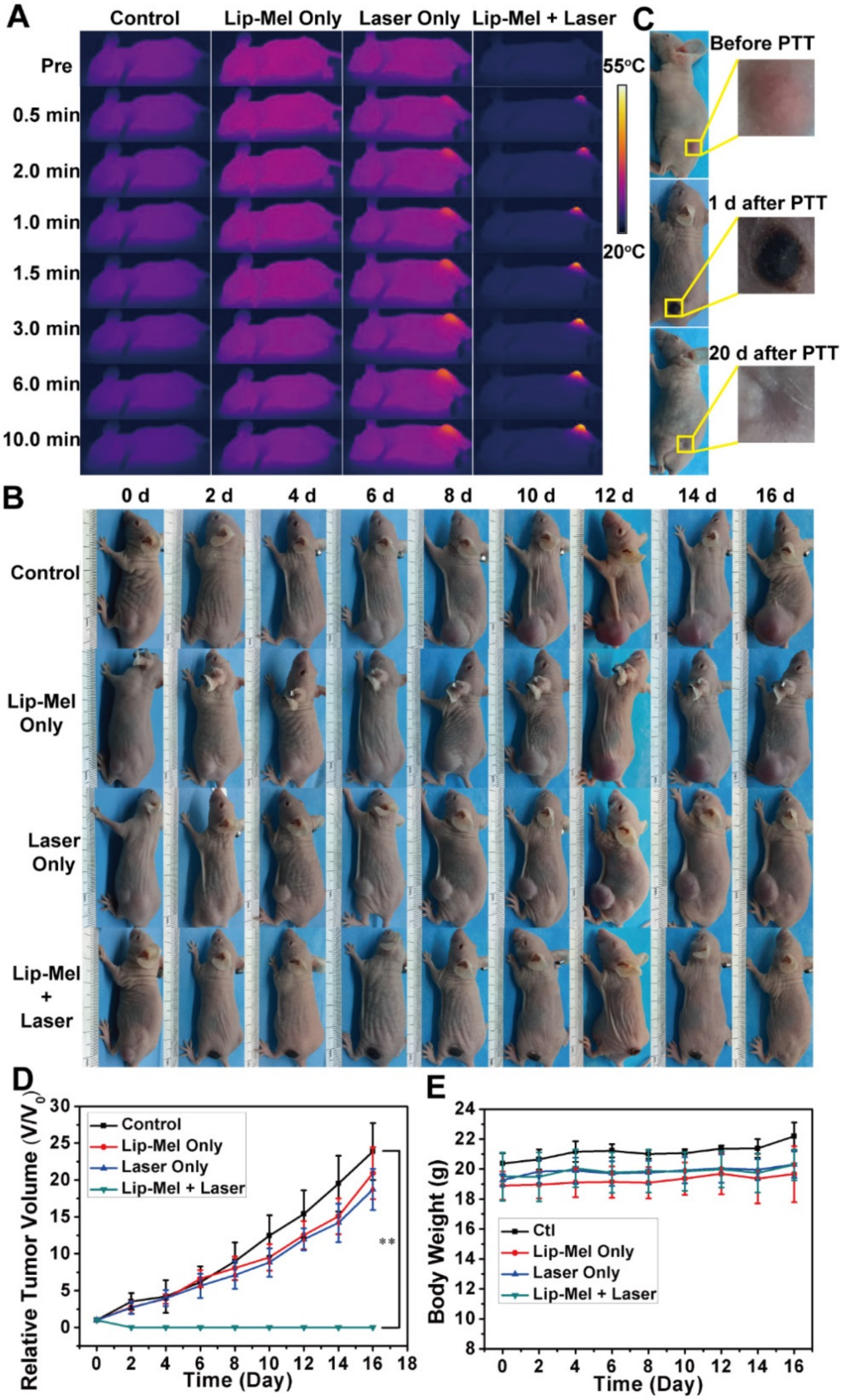

Figure 8. *In vivo* PTT efficiency of Lip-Mel upon external NIR irradiation. (**A**) IR thermal images of MDA-MB-231 tumor-bearing mice of the four groups (control, Lip-Mel only, Laser only and Lip-Mel + Laser group) taken at different times. (**B**) Photographs of MDA-MB-231 tumor-bearing mice in the four groups taken during a 16-day period after the various treatments. (**C**) Photographs of MDA-MB-231 tumor-bearing mouse and the tumor region before, 1 day and 20 days after PTT with the Lip-Mel assistance. (**D**) Tumor growth curves (n = 5, mean ± SD, $^{**}P < 0.01$) of four groups after various treatments. (**E**) Body-weight curves (n = 5, mean ± SD) of the four groups after different treatments.

To detect *in vivo* toxicity of PTT assisted by Lip-Mel, H&E staining of the main organs (heart, liver, spleen, lung and kidney) was performed, which showed no obvious histopathological lesion. Negligible weight fluctuations **(Figure 8E)** and H&E staining of the main organs **(Figure 9A)** demonstrated few adverse effects of PTT on the health and normal organs of the mice. H&E and TUNEL staining on tumor sections further confirmed serious necrosis of tumor in the Lip-Mel + Laser group as compared to the other three groups **(Figure 9B)**. As shown in H&E-stained tumor sections, there were only a small portion of purple blue (normal nucleus) and many more deformed nuclei (karyopyknosis, karyorrhexis and karyolysis) in the Lip-Mel + Laser group, indicating the high apoptosis and coagulative necrosis of the cancer cells. From the TUNEL assay result, representative apoptosis-positive cells were indicated by dark-brown nuclei in the Lip-Mel + Laser group. Immunochemical staining of Ki-67 on tumor sections showed the *in vivo* proliferative activities of the four groups, where proliferative cells were stained brown. The Lip-Mel + Laser group exhibited a significant suppression effect (the least brown nuclei) on tumor cell proliferation while the other three groups showed almost no killing effects on the proliferative activity of tumor cells.

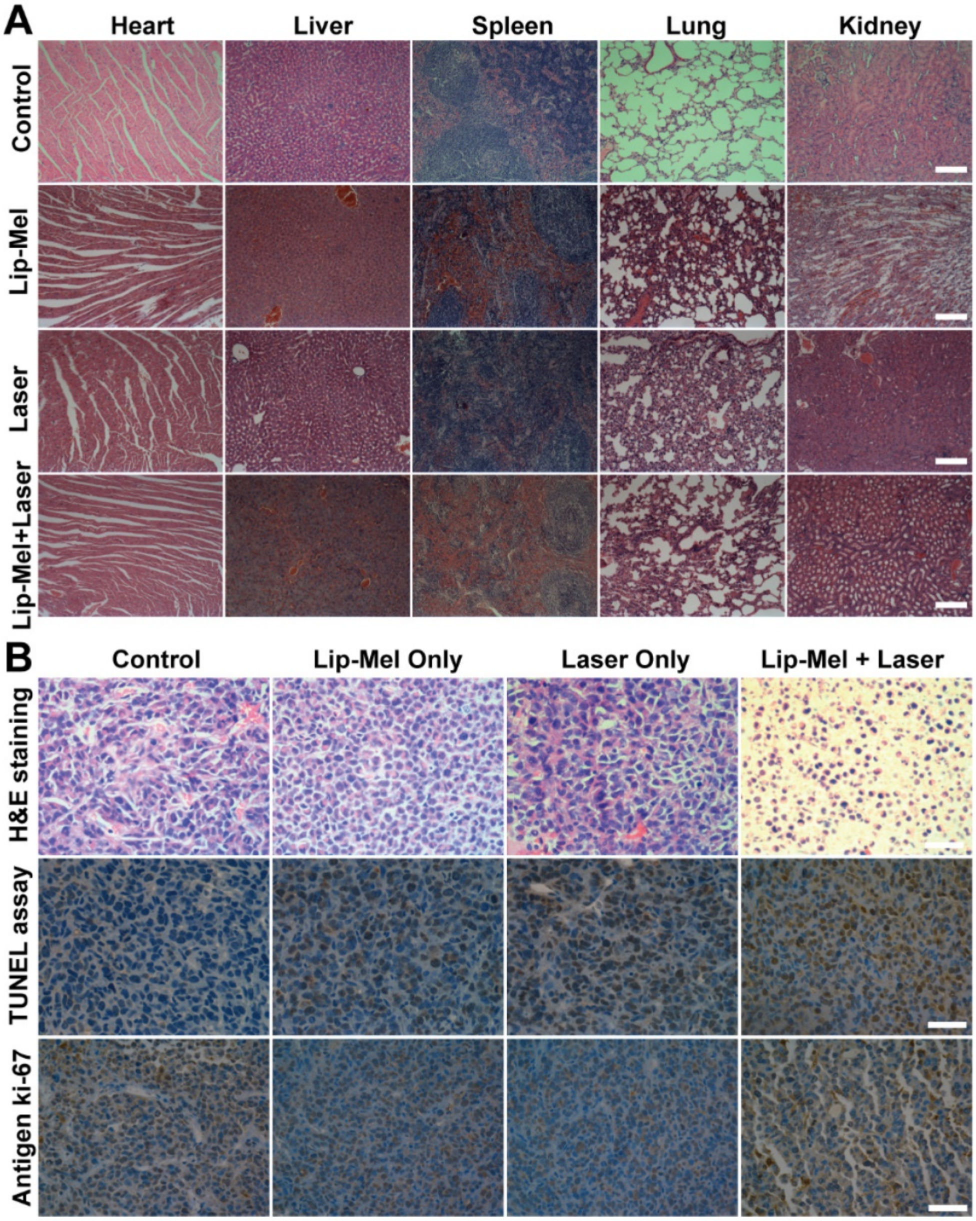

Figure 9. (**A**) H&E staining of the major organs (heart, liver, spleen, lung and kidney) of MDA-MB-231 tumor-bearing nude mice after various treatments. All the scale bars are 100 μm. (**B**) H&E staining, TUNEL staining and immunochemical staining of Ki-67 on tumor sections after various treatments. All the scale bars are 50 μm.

Conclusions

In summary, we successfully constructed, for the first time, a multifunctional melanin-based theranostic nanoliposome (Lip-Mel) for highly efficient PA/MR imaging-guided photothermal ablation of tumor, which was systematically demonstrated both *in vitro* and *in vivo*. These multifunctional liposomes are promising for clinical translation because their components, lipid and melanin, originate from human body, which can guarantee their high biocompatibility and high biosafety for theranostic applications. In particular, the efficient encapsulation of melanin into PEGylated liposomes was demonstrated to assuage the potential toxicity of melanin and improve the photothermal performance of encapsulated melanin. The high performance of the as-designed Lip-Mel as a contrast agent for concurrent PAI and MRI was solidly demonstrated in tumor-bearing mice, providing potential for the guidance and monitoring of the therapeutic process and outcome. In particular, the high photothermal conversion efficiency of the as-prepared Lip-Mel achieved the complete eradication of tumors in breast cancer-bearing mice, showing the high performance of Lip-Mel for the photothermal ablation of tumors. Therefore, this work paves a new way for developing novel theranostic agents with concurrent high biosafety and desirable theranostic performance, through the use of materials that totally originate from biosystems.

Abbreviations

ALT: alanine aminotransferase; AST: aminotransferase; BUN: blood urea nitrogen; Calcein-AM: Calcein acetoxymethyl ester; CCK-8: Cell Counting Kit-8; CK: creatine kinase; CLSM: confocal laser scanning microscope; CR: creatinine; DAPI: 2-(4-Amidinophenyl)-6-indolecarbamidinedihydrochloride; DiI: 1,1'-dioctadecyl-3,3,3',3'-tetramethylindocarbocyanine perchlorate; DiR: 1,1′-dioctadecyl-3,3,3′,3′-tetramethylindotricarbocyanine iodide; DLS: dynamic light scattering; DMEM: Dulbecco's Modified Eagle Medium; EPR: enhanced permeability and retention; FBS: fetal bovine serum; H&E: hematoxylin and eosin; IR: infrared radiation; LDH-L: L-lactate dehydrogenase; Lip: liposomes; PBS: phosphate buffered saline; Lip-Mel: melanin-based nanoliposome; MR: magnetic resonance; MRI: magnetic resonance imaging; NIR: near infrared; PA: photoacoustic; PAI: photoacoustic imaging; PI: propidium iodide; PSII: the percentage of signal intensity increase; PTT: Photothermal therapy; ROI: region of interest; SI: signal intensity; SIr: Relative signal intensity; TBIL: total bilirubin; TUNEL: TdT-mediated dUTP Nick-End Labeling.

Acknowledgement

We greatly acknowledge the financial support from the National Key R&D Program of China (Grant No. 2016YFA0203700), National Natural Science Foundation of China (Grant No. 81571688, 81771845, 81371718, 51722211, 51672303), Young Elite Scientist Sponsorship Program by CAST (Grant No. 2015QNRC001) and Chongqing Foundation and Cutting-edge Research Projects (cstc2014jcyjA10013).

Supplementary Material

Supplementary figures.
http://www.thno.org/v08p1591s1.pdf

Competing Interests

The authors have declared that no competing interest exists.

References

1. Chen H, Zhang W, Zhu G, Xie J, Chen X. Rethinking Cancer Nanotheranostics. Nat Rev Mater. 2017; 2: 17024.
2. Chen Y, Wu Y, Sun B, Liu S, Liu H. Two-Dimensional Nanomaterials for Cancer Nanotheranostics. Small. 2017; 13: 1603446.
3. Ji T, Zhao Y, Ding Y, Nie G. Using Functional Nanomaterials to Target and Regulate the Tumor Microenvironment: Diagnostic and Therapeutic Applications. Adv Mater. 2013; 25: 3508-25.
4. Zhou Y, Jing X, Chen Y. Material Chemistry of Graphene Oxide-Based Nanocomposites for Theranostic Nanomedicine. J Mater Chem B. 2017; 5: 6451-70.
5. Pang X, Tan X, Wang J, Liu L, You Q, Sun Q, et al. Hollow Au-Cu Nanocomposite for Real-Time Tracing Photothermal/Antiangiogenic Therapy. Adv Healthc Mater. 2017; 6: 1700099.
6. Kim JW, Galanzha EI, Shashkov EV, Moon HM, Zharov VP. Golden Carbon Nanotubes as Multimodal Photoacoustic and Photothermal High-contrast Molecular Agents. Nat Nanotechnol. 2009; 4: 688-94.
7. Wu YZ, Sun J, Zhang Y, Pu M, Zhang G, He N, et al. Effective Integration of Targeted Tumor Imaging and Therapy Using Functionalized InP QDs with VEGFR2 Monoclonal Antibody and miR-92a Inhibitor. ACS Appl Mater Interfaces. 2017; 9: 13068-78.
8. Ge J, Lan M, Zhou B, Liu W, Guo L, Wang H, et al. A Graphene Quantum Dot Photodynamic Therapy Agent with High Singlet Oxygen Generation. Nat Commun. 2014; 5: 4596.
9. Jian J, Liu C, Gong Y, Su L, Zhang B, Wang Z, et al. India Ink Incorporated Multifunctional Phase-transition Nanodroplets for Photoacoustic/Ultrasound Dual-modality Imaging and Photoacoustic Effect Based Tumor Therapy. Theranostics. 2014; 4: 1026-38.
10. Fan CH, Cheng YH, Ting CY, Ho YJ, Hsu PH, Liu HL, et al. Ultrasound/Magnetic Targeting with SPIO-DOX-Microbubble Complex for Image-Guided Drug Delivery in Brain Tumors. Theranostics. 2016; 6: 1542-56.
11. Espinosa A, Di Corato R, Kolosnjaj-Tabi J, Flaud P, Pellegrino T, Wilhelm C. Duality of Iron Oxide Nanoparticles in Cancer Therapy: Amplification of Heating Efficiency by Magnetic Hyperthermia and Photothermal Bimodal Treatment. ACS Nano. 2016; 10: 2436-46.
12. Augustine S, Singh J, Srivastava M, Sharma M, Das A, Malhotra BD. Recent Advances in Carbon Based Nanosystems for Cancer Theranostics. Biomaterials Sci. 2017; 5: 901-52.
13. Liu Z, Tabakman S, Welsher K, Dai H. Carbon Nanotubes in Biology and Medicine: In Vitro and In Vivo Detection, Imaging and Drug Delivery. Nano Res. 2009; 2: 85-120.
14. Dong Z, Gong H, Gao M, Zhu W, Sun X, Feng L, et al. Polydopamine Nanoparticles as a Versatile Molecular Loading Platform to Enable Imaging-guided Cancer Combination Therapy. Theranostics. 2016; 6: 1031-42.
15. Liang X, Fang L, Li X, Zhang X, Wang F. Activatable Near Infrared Dye Conjugated Hyaluronic Acid Based Nanoparticles as a Targeted Theranostic Agent for Enhanced Fluorescence/CT/Photoacoustic Imaging Guided Photothermal Therapy. Biomaterials. 2017; 132: 72-84.
16. Cheng Y, Cheng H, Jiang C, Qiu X, Wang K, Huan W, et al. Perfluorocarbon Nanoparticles Enhance Reactive Oxygen Levels and Tumour Growth Inhibition in Photodynamic Therapy. Nat Commun. 2015; 6: 8785.

17. Antaris AL, Chen H, Cheng K, Sun Y, Hong G, Qu C, et al. A Small-molecule Dye for NIR-II imaging. Nat Mater. 2016; 15: 235-42.
18. Zhang XD, Wu D, Shen X, Liu PX, Yang N, Zhao B, et al. Size-dependent In Vivo Toxicity of PEG-Coated Gold Nanoparticles. Int J Nanomedicine. 2011; 6: 2071-81.
19. Bussy C, Methven L, Kostarelos K. Hemotoxicity of Carbon Nanotubes. Adv Drug Deliv Rev. 2013; 65: 2127-34.
20. Wan S, Zhang LQ, Wang S, Liu Y, Wu CC, Cui C, et al. Molecular Recognition-Based DNA Nanoassemblies on the Surfaces of Nanosized Exosomes. J Am Chem Soc. 2017; 139: 5289-92.
21. Rea I, Terracciano M, De Stefano L. Synthetic vs Natural: Diatoms Bioderived Porous Materials for the Next Generation of Healthcare Nanodevices. Adv Healthc Mater. 2017; 6: 1601125.
22. Lovell JF, Jin CS, Huynh E, Jin H, Kim C, Rubinstein JL, et al. Porphysome Nanovesicles Generated by Porphyrin Bilayers for Use as Multimodal Biophotonic Contrast Agents. Nat Mater. 2011; 10: 324-32.
23. Starnatas GN, Zmudzka BZ, Kollias N, et al. Non-Invasive Measurements of Skin Pigmentation in Situ. Pigment Cell Res. 2004; 17: 618-26.
24. ElObeid AS, Kamal-Eldin A, Abdelhalim MAK, Haseeb AM. Pharmacological Properties of Melanin and Its Function in Health. Basic Clin Pharmacol Toxicol. 2017; 120: 515-22.
25. Jathoul AP, Laufer J, Ogunlade O, Treeby B, Cox B, Zhang E, et al. Deep In Vivo Photoacoustic Imaging of Mammalian Tissues Using a Tyrosinase-based Genetic Reporter. Nat Photon. 2015; 9: 515-22.
26. Lin J, Wang M, Hu H, Yang X, Wen B, Wang Z, et al. Multimodal-Imaging-Guided Cancer Phototherapy by Versatile Biomimetic Theranostics with UV and Gamma-Irradiation Protection. Adv Mater. 2016; 28: 3273-9.
27. Zhang R, Fan Q, Yang M, Cheng K, Lu X, Zhang L, et al. Engineering Melanin Nanoparticles as An Efficient Drug-Delivery System for Imaging-Guided Chemotherapy. Adv Mater. 2015; 27: 5063-9.
28. Kuya K, Shinohara Y, Miyoshi F, Fujii S, Tanabe Y, Ogawa T. Correlation between Neuromelanin-sensitive MR Imaging and (123)I-FP-CIT SPECT in Patients with Parkinsonism. Neuroradiology. 2016; 58: 351-6.
29. Cho S, Park W, Kim DH. Silica-Coated Metal Chelating-Melanin Nanoparticles as a Dual-Modal Contrast Enhancement Imaging and Therapeutic Agent. ACS Appl Mater Interfaces. 2017; 9: 101-11.
30. Yang K, Hu L, Ma X, Ye S, Cheng L, Shi X, et al. Multimodal Imaging Guided Photothermal Therapy Using Functionalized Graphene Nanosheets Anchored with Magnetic Nanoparticles. Adv Mater. 2012; 24: 1868-72.
31. Shao J, Xie H, Huang H, Li Z, Sun Z, Xu Y, et al. Biodegradable Black Phosphorus-Based Nanospheres for In Vivo Photothermal Cancer Therapy. Nat Commun. 2016; 7: 12967.
32. Lin H, Wang X, Yu L, Chen Y, Shi J. Two-Dimensional Ultrathin MXene Ceramic Nanosheets for Photothermal Conversion. Nano Lett. 2017; 17: 384-91.
33. Liu Y, Ai K, Liu J, Deng M, He Y, Lu L. Dopamine-Melanin Colloidal Nanospheres: An Efficient Near-Infrared Photothermal Therapeutic Agent for In Vivo Cancer Therapy. Adv Mater. 2013; 25: 1353-9.
34. Li N, Zhang CX, Wang XX, Zhang L, Ma X, Zhou J, et al. Development of Targeting Lonidamine Liposomes that Circumvent Drug-Resistant Cancer by Acting on Mitochondrial Signaling Pathways. Biomaterials. 2013; 34: 3366-80.
35. Yu Y, Wang ZH, Zhang L, Yao HJ, Zhang Y, Li RJ, et al. Mitochondrial Targeting Topotecan-Loaded Liposomes for Treating Drug-Resistant Breast Cancer and Inhibiting Invasive Metastases of Melanoma. Biomaterials. 2012; 33: 1808-20.
36. Brigger I, Dubernet C, Couvreur P. Nanoparticles in Cancer Therapy and Diagnosis. Adv Drug Deliv Rev. 2012; 64: 24-36.
37. Barenholz Y. Doxil(R)--the First FDA-Approved Nano-Drug: Lessons Learned. J Control Release. 2012; 160: 117-34.
38. Newman MS, Colbern GT, Working PK, Engbers C, Amantea MA. Comparative Pharmacokinetics, Tissue Distribution, and Therapeutic Effectiveness of Cisplatin Encapsulated in Long-Circulating, Pegylated Liposomes (SPI-077) in Tumor-Bearing Mice. Cancer Chemother Pharmacol. 1999; 43: 1-7.
39. Valluru KS, Wilson KE, Willmann JK. Photoacoustic Imaging in Oncology: Translational Preclinical and Early Clinical Experience. Radiology. 2016; 280: 332-49.
40. De la Zerda A, Zavaleta C, Keren S, Vaithilingam S, Bodapati S, Liu Z, et al. Carbon Nanotubes as Photoacoustic Molecular Imaging Agents in Living Mice. Nat Nanotechnol. 2008; 3: 557-62.
41. Zhang HF, Maslov K, Stoica G, Wang LV. Functional Photoacoustic Microscopy for High-Resolution and Noninvasive In Vivo Imaging. Nat Biotechnol. 2006; 24: 848-51.
42. Zhou Y, Li G, Zhu LR, Li CY, Cornelius LA, Wang LHV. Handheld Photoacoustic Probe to Detect both Melanoma Depth and Volume at High sSpeed In Vivo. J Biophotonics. 2015; 8: 961-7.
43. Xu G, Xue YF, Ouml;zkurt ZG, Slimani N, Hu ZZ, Wang XD, et al. Photoacoustic Imaging Features of Intraocular Tumors: Retinoblastoma and Uveal Melanoma. PLoS One. 2017; 12: 15.
44. Woodruff WW, Jr., Djang WT, McLendon RE, Heinz ER, Voorhees DR. Intracerebral Malignant Melanoma: High-Field-Strength MR Imaging. Radiology. 1987; 165: 209-13.
45. Bekiesinska-Figatowska M, Sawicka E, Zak K, Szczygielski O. Age Related Changes in Brain MR Appearance in the Course of Neurocutaneous Melanosis. Eur J Radiol. 2016; 85: 1427-31.
46. Stritzker J, Kirscher L, Scadeng M, Deliolanis NC, Morscher S, Symvoulidis P, et al. Vaccinia Virus-Mediated Melanin Production Allows MR and Optoacoustic Deep Tissue Imaging and Laser-Induced Thermotherapy of Cancer. Proc Natl Acad Sci U S A. 2013; 110: 3316-20.
47. Ni D, Zhang J, Wang J, Hu P, Jin Y, Tang Z, et al. Oxygen Vacancy Enables Markedly Enhanced Magnetic Resonance Imaging-Guided Photothermal Therapy of a Gd^{3+}-Doped Contrast Agent. ACS Nano. 2017; 11: 4256-64.
48. Wang LV. Multiscale Photoacoustic Microscopy and Computed Tomography. Nat Photon. 2009; 3: 503-9.
49. Jokerst JV, Thangaraj M, Kempen PJ, Sinclair R, Gambhir SS. Photoacoustic Imaging of Mesenchymal Stem Cells in Living Mice via Silica-Coated Gold Nanorods. Acs Nano. 2012; 6: 5920-30.
50. Mallidi S, Larson T, Tam J, Joshi PP, Karpiouk A, Sokolov K, et al. Multiwavelength Photoacoustic Imaging and Plasmon Resonance Coupling of Gold Nanoparticles for Selective Detection of Cancer. Nano Lett. 2009; 9: 2825-31.
51. Yu J, Yang C, Li J, Ding Y, Zhang L, Yousaf MZ, et al. Multifunctional Fe_5C_2 Nanoparticles: A Targeted Theranostic Platform for Magnetic Resonance Imaging and Photoacoustic Tomography-Guided Photothermal Therapy. Adv Mater. 2014; 26: 4114-20.
52. Lim D-K, Barhoumi A, Wylie RG, Reznor G, Langer RS, Kohane DS. Enhanced Photothermal Effect of Plasmonic Nanoparticles Coated with Reduced Graphene Oxide. Nano Lett. 2013; 13: 4075-9.
53. Chen H, Xiao L, Anraku Y, Mi P, Liu X, Cabral H, et al. Polyion Complex Vesicles for Photoinduced Intracellular Delivery of Amphiphilic Photosensitizer. J Am Chem Soc. 2014; 136: 157-63.
54. Miranda D, Carter K, Luo D, Shao S, Geng J, Li C, et al. Multifunctional Liposomes for Image-Guided Intratumoral Chemo-Phototherapy. Adv Healthc Mater. 2017; 6: 1700253.
55. Guo W, Guo C, Zheng N, Sun T, Liu S. Cs_xWO_3 Nanorods Coated with Polyelectrolyte Multilayers as a Multifunctional Nanomaterial for Bimodal Imaging-Guided Photothermal/Photodynamic Cancer Treatment. Adv Mater. 2017; 29: 1604157.
56. Shibu ES, Hamada M, Murase N, Biju V. Nanomaterials Formulations for Photothermal and Photodynamic Therapy of Cancer. J Photochem and Photobiol C. 2013; 15: 53-72.